journal of the mechanical behavior of biomedical materials 134 (2022) 105405

Contents lists available at ScienceDirect

Journal of the Mechanical Behavior of Biomedical Materials

journal homepage: www.elsevier.com/locate/jmbbm

Assessing minipig compact jawbone quality at the microscale

Tatiana Kochetkova [a,*], Alexander Groetsch [a], Michael Indermaur [b], Cinzia Peruzzi [a], Stefan Remund [c], Beat Neuenschwander [c], Benjamin Bellon [d,e], Johann Michler [a], Philippe Zysset [b], Jakob Schwiedrzik [a,**]

[a] Empa, Swiss Federal Laboratories for Materials Science and Technology, Thun, Switzerland
[b] ARTORG Center for Biomedical Engineering Research, University of Bern, Switzerland
[c] Institute for Applied Laser, Photonics and Surface Technologies (ALPS), Bern University of Applied Sciences, Burgdorf, Switzerland
[d] Institut Straumann AG, Basel, Switzerland
[e] Department of Periodontology, Faculty of Dentistry, University of Zürich, Zürich, Switzerland

ARTICLE INFO

Keywords:
Animal model
Miniature pig
Mandible
Micro-CT
Raman spectroscopy
Nanoindentation
Femtosecond laser ablation
Micropillar compression
Structure-property relationships

ABSTRACT

Preclinical studies often require animal models for *in vivo* experiments. Particularly in dental research, pig species are extensively used due to their anatomical similarity to humans. However, there is a considerable knowledge gap on the multiscale morphological and mechanical properties of the miniature pigs' jawbones, which is crucial for implant studies and a direct comparison to human tissue. In the present work, we demonstrate a multimodal framework to assess the jawbone quantity and quality for a minipig animal model that could be further extended to humans.

Three minipig genotypes, commonly used in dental research, were examined: Yucatan, Göttingen, and Sinclair. Three animals per genotype were tested. Cortical bone samples were extracted from the premolar region of the mandible, opposite to the teeth growth. Global morphological, compositional, and mechanical properties were assessed using micro-computed tomography (micro-CT) together with Raman spectroscopy and nanoindentation measurements, averaged over the sample area. Local mineral-mechanical relationships were investigated with the site-matched Raman spectroscopy and micropillar compression tests. For this, a novel femtosecond laser ablation protocol was developed, allowing high-throughput micropillar fabrication and testing without exposure to high vacuum.

At the global averaged sample level, bone relative mineralization demonstrated a significant difference between the genotypes, which was not observed from the complementary micro-CT measurements. Moreover, bone hardness measured by nanoindentation showed a positive trend with the relative mineralization. For all genotypes, significant differences between the relative mineralization and elastic properties were more pronounced within the osteonal regions of cortical bone. Site-matched micropillar compression and Raman spectroscopy highlighted the differences between the genotypes' yield stress and mineral to matrix ratios.

The methods used at the global level (averaged over sample area) could be potentially correlated to the medical tools used to assess jawbone toughness and morphology in clinics. On the other hand, the local analysis methods can be applied to quantify compressive bone mechanical properties and their relationship to bone mineralization.

1. Introduction

Clinical assessment of the jawbone quality. Bone quality is often referred to as the determining parameter for dental implant studies. The term bone quality stands for the combination of various bone physiological, compositional, mechanical, and structural parameters (Compston, 2006; Recker and Janet Barger-Lux, 2004). All of these bone properties are responsible, to a different extent, for bone fracture resistance and implant stability (Merheb et al., 1111; Ovesy et al., 2018; Voumard et al., 2019). While the direct assessment of bone quality has

* Corresponding author.
** Corresponding author.
E-mail addresses: tatiana.kochetkova@empa.ch (T. Kochetkova), jakob.schwiedrzik@empa.ch (J. Schwiedrzik).

https://doi.org/10.1016/j.jmbbm.2022.105405
Received 24 May 2022; Received in revised form 21 July 2022; Accepted 26 July 2022
Available online 1 August 2022

not been established yet due to the complicated interrelationships between the bone parameters, indirect estimation of bone quantity in clinics relies to a greater extent on the bone mineral density measurements (Molly, 2006; Turkyilmaz, 2011).

Jawbone mineral density is often assessed during preoperative imagining techniques like intraoral or panoramic radiographs (Nackaerts et al., 2007; White et al., 2005; Graham, 2015) and quantitative computed tomography (Shahlaie et al., Crigger; Stoppie et al., 2005). A variation of the latter, cone beam computed tomography is emerging as the most common imaging method employed in clinical practice (Aranyarachkul et al., Crigger; Scarfe et al., 2006; Jacobs et al., 2018; Baumgaertel et al., 2009; Hua et al., 2009). Another method for the estimation of the bone mineral density is dual-energy X-ray absorptiometry (DXA). While it is widely used in bone density assessment at the spine, hip, and/or lower arm sites, it has been used solely in experimental settings for jawbone density evaluations (Nackaerts et al., 2007; von Wowern, 2001).

Despite the recent advances in imagining techniques, the most widely used approach for jawbone quality assessment in clinics still follows the grading system introduced by Lekholm and Zarb (Lekholm et al., 1985). According to their classification, the bone quality is graded from 1 to 4 based on the tactile sensation of the surgeon during drilling. This subjective approach is often combined with imaging techniques and/or other methods related to primary and secondary implant stability, like the torque force measurements during the implant insertion (Fuster-Torres et al., 1051; Lee et al., Crigger; Meredith, 1998; Alsaadi et al., 2007; Oh and Kim, 2012). There is a potential need to support this grading system with less invasive and quantitative methods (Ribeiro-Rotta et al., 2011; Norton and Gamble, 2001).

Laboratory methods used in the current study to assess jawbone quality. Defining other possible bone biomarkers describing bone quality would improve the current clinical methods used for bone quality assessment. Laboratory-based techniques like nanoindentation, micropillar compression, microscale computed tomography, and Raman spectroscopy are attractive experimental techniques that allow the mechanical, morphological, and compositional analysis of microscale bone volumes.

Nanoindentation is an accepted method to probe local elastic properties, where a hard and sharp tip (typically made of diamond) with a well-defined shape is driven into a flat surface of the sample while tip displacement and reaction forces are being measured. The hardness and elastic modulus of the material can be extracted following the pioneering work of Oliver and Pharr (1992). The nanoindentation technique was first applied in dental research on hard tissues like enamel and dentin in the early 1990s (Van Meerbeek et al., 1993; Angker and Swain, 2006). Twenty years later, nanoindentation was used in jawbone characterization near implant sites, and recently in quality assessment in mice jawbone (Watanabe et al., 2020).

Micropillar compression is a relatively new experimental technique introduced by Uchic et al. in the early 2000s (Uchic and Dimiduk, 2005). The methodology is similar to nanoindentation, but instead of a sharp tip, a flat punch compresses a small volume of material with a defined geometry. This produces a uniform stress field in the tested volume so that both elastic and yield properties of the material can be extracted, giving insights into the plastic deformation behavior of the material. The first micropillar compression of bone was done in the mid-2010s (Schwiedrzik et al., 2014, 2017) on ovine tibial bone. More recently, this method was also applied to the human bone biopsies (Tertuliano and Greer, 2016; Indermaur et al., 2021). Using a portable micro-indenter setup further allows to combine it in a multi-modal approach including synchrotron radiation providing information on multiple length scales (Groetsch et al., 2019).

Similar to computed tomography used in clinics, microscale computed tomography (micro-CT), developed in the early 1980s (Feldkamp et al., 2009), is commonly used to visualize and analyze sample morphology and mineral density. However, clinical CT scanners can typically resolve about 1 mm, while micro-CT systems can reach resolutions of 1–5 μm (Kuhn et al., 1990; V Swain and Xue, 2009). This allows for studying bone mineral density and morphology at a high spatial resolution. Recently phase-contrast nanometer computed tomography was employed to image single mineralized collagen fibers at a voxel size of $(20\ nm)^3$. The high sensitivity of the technique for light elements as found in biological materials allowed it to distinguish features down to the fibril level (Groetsch et al., 2021).

Raman spectroscopy is a well-known technique in bone and dental research. In principle, Raman spectroscopy allows the detection of frequency shifts of inelastically scattered light coming from the specimen exposed to a monochromatic light source, commonly a laser. These Raman shifts are assigned to characteristic chemical bonds, giving information on the material composition. Since the first report of Raman spectra of a tooth in 1974 (O'Shea et al., 1974), this technique was used extensively in scientific studies of enamel and dentin (Leroy et al., 2002; Salehi et al., 2012; Wang et al., 2007a).

Animal models. It is common nowadays to investigate biological phenomena on animal models, due to practical, ethical, and economical reasons (Hau, 2008). Animal models promote the research in bone tissue engineering and modelling (McGovern et al., 2018), as well as bone metastasis (Rosol et al., 2003; Simmons et al., 2015) and repair processes (An and Friedman, 2020). Pig species exhibit many anatomical and physiological similarities with humans, making them an attractive choice for preclinical experimentation in various medical and biomedical fields (Kobayashi et al., 2012; Vodička et al., 2005; Litten-Brown et al., 2010). In particular, miniature pig species (minipigs) were specifically developed for research purposes and are now extensively used for *in vivo* experiments prior to translation to humans (Rozkot et al., 2015; Peter et al., 2011; Nunoya et al., 2007). While keeping the resemblance to humans, minipigs have convenient body dimensions and well-controlled genetics, which facilitates the handling and maintenance of these animals in the laboratory (Vodička et al., 2005; Rozkot et al., 2015). Miniature pigs were first used in dental research several decades ago (Weaver et al., 1962). The facial and oral regions of minipigs exhibit similar physiology and development as that of humans (Wang et al., 2007b). Moreover, miniature pigs possess both permanent and deciduous sets of teeth and perform both chewing and biting jaw actions, like humans (Weaver et al., 1962). All of this, together with the low purchase and maintenance costs, makes minipigs an excellent animal model for various studies in dental research (Wang et al., 2007b; Ruehe et al., 2009; Buser et al., 1991). Miniature pig models are already reported in bone regeneration (Ruehe et al., 2009), osseointegration (Kuo et al., 2017), and bone fracture healing during implantation (Imwinkelried et al., 2020). Nevertheless, there is a considerable knowledge gap on the multiscale morphological and mechanical properties of the miniature pigs' jawbones, which is crucial for implant studies and a direct comparison to human tissue.

Study outline. Here, we report a multimodal approach to assess jawbone quantity and quality at the microscale. For this, we used an established animal model for dental research: the miniature pig. Three minipig genotypes were examined: Yucatan, Göttingen, and Sinclair. Through the combination of laboratory-based methods, we assessed bone mineralization, morphology, and mechanical properties on the local and global average levels. Microscale computed tomography, Raman spectroscopy, and nanoindentation were employed for sample characterization at the global level, averaged over the sample area. Nanoindentation gave assess to the elastic properties of the cortical jawbone, while micro-CT and Raman spectroscopy to bone morphology and mineralization. To the best of our knowledge, this is the first study where Raman spectroscopy was applied to investigate the jawbone relative mineralization. At the local level, micropillar compression was used for the first time on the compact jawbone, to extract yield and elastic bone properties, which are critical in dental research. For the first time, micropillar compression tests were carried out on laser-fabricated bone micropillars, which enables high throughput mechanical

characterization. Following our previous study (Kochetkova et al., 2021), we combined Raman spectroscopy and micropillar compression measurements in a site-matched manner to estimate the mechanical properties of bone in correlation with the local bone mineralization level, giving access to structure-property relationships at the microscale.

2. Materials and methods

2.1. Sample preparation

Jaw samples from skeletally mature minipigs of three genotypes (Yucatan, Göttingen, and Sinclair) of age between 23 and 27 months were obtained from Institut Straumann AG (Basel, Switzerland). The samples were obtained from dental studies after their completion and stored in formalin before further preparation. In total, three animals per genotype were used (N = 9). The coronal cross-section of the mandibular premolar region was dissected from the rest of the jaw with a diamond band saw under constant water irrigation (Exakt, Norderstedt, Reichert-Jung). The cortical bone region, adjacent to the inferior border of the mandible, was further sectioned from the jawbone slice. The resulting bone pieces of about 3 mm in height and 4 × 4 mm in width x depth were mechanically cleaned and dried at ambient conditions for 24 h. The pieces were then glued onto an aluminium SEM stub with a 2-component epoxy resin adhesive (Schnellfest, UHU, Germany) so that the sample top surface followed the coronal plane from the mandibular cross-section. Finally, the exposed specimen surfaces were polished with progressive grades of silicon carbide paper and finished manually on a soft cloth with a 1 μm diamond suspension followed by a 0.04 μm SiO_2 suspension.

2.2. Micromechanical characterization

2.2.1. Nanoindentation

Nanoindentation maps were carried out using a Hysitron Ubi-1 nanomechanical testing system equipped with a Berkovich diamond tip. Measurements were performed at room temperature and ambient pressure and humidity. Nanoindentation maps consisted of 2x3 indents with a 20 μm step size, avoiding indentions in the vicinity of the deformation zone while being placed within the zones of interest, specifically osteons. Each indentation was performed under load–control mode with 10 mN maximum load and the following segment times: 20 s loading, 30 s holding at peak-load, and 20 s unloading segment. An additional 60 s waiting time was added between each indent to reduce instrument drift. Indentation maps were located either in the osteonal, interstitial, or plexiform regions. In total 10 maps for each region of interest were collected per animal sample resulting in 120–180 indents per sample. Indentation maps were distributed across the sample surface, consequently providing information on average elastic bone properties at the whole sample level.

2.2.2. Micropillar fabrication via femtosecond laser ablation

A novel laser ablation protocol was developed based on femtosecond (fs) laser ablation to prepare a micropillar array on each of the bone samples (Lim et al., 2009). Fabrication of micropillars on the sample surface was done using a femtosecond-pulsed laser (SATSUMA HPII, Amplitudes Systemes) at 515 nm wavelength with 320–350 fs pulse duration and 3 kHz repetition frequency, with an average laser power of 12 mW. The resulting laser pulse energy and peak fluence were 3.96 μJ and 5.14 J/cm^2 accordingly. The ablation was done in a unidirectional scanning mode at 15 mm/s, enabling low heat accumulation (Appendix 1). An array of 5x5 micropillars was ablated on each sample surface for further mechanical testing (Fig. 1). The dimensions of the micropillars were estimated from high-resolution scanning electron microscopy (HRSEM) images taken at an acceleration voltage of 1.5 kV (Hitachi S-4800, Japan). On average, the pillar diameter was 24 ± 3 μm with an aspect ratio of 2.3 ± 0.3 and a taper angle of 15° ± 2°.

2.2.3. Micropillar compression

Micropillar compressions were performed using an ex-situ indenter setup developed in-house based on commercial hardware for actuation, sensing, and electronics (Alemnis AG, Switzerland) (Kochetkova et al., 2021; Peruzzi et al., 2021). Experiments were performed at ambient temperature and humidity with a flat punch indenter tip (60 μm diameter). Samples were compressed uniaxially using a quasi-static displacement-controlled loading protocol at a strain rate of 10^{-3} s^{-1} and up to 15% of engineering strain. Two types of protocol were used: (i) monotonic and (ii) cyclic loading. The latter included repetitive segments of 750 nm loading and 250 nm partial unloading. The typical

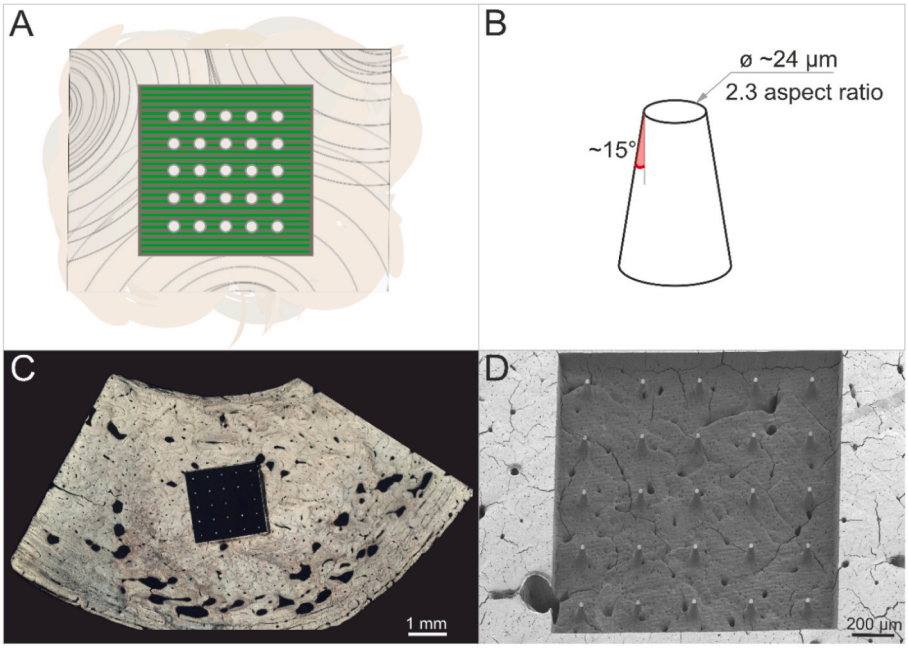

Fig. 1. Schematic of the laser ablation of bone in a unidirectional scanning mode with marked micropillar array positions (A) and the output micropillar geometry (B); optical overview image of the sample top surface with femtosecond laser ablated micropillar array (C); close-up SEM image of the micropillar array (D).

stress-strain curves for two testing protocols are presented in the graphical abstract. From both protocols, yield stress and strain were extracted, whereas from the cyclic loading protocol the elastic moduli were additionally extracted from the unloading segments, prior to the yield point. Yield stress in each stress-strain curve was computed as the stress that is needed for plastic deformation of 0.2%. On average, 20 micropillars were tested per animal sample, of which 5 were cyclically loaded.

Data analysis was done in Python v3.8 (van Rossum and Drake, 2009) using an in-house script following the methodology of Schwiedrzik et al. (2014) with the modified Sneddon approach of Zhang et al. (2006) for substrate compliance corrections. The influence of the taper angle on the output mechanical properties was corrected using finite element simulations in Abaqus/CAE (Dassault Systemes Simulia Corp., Johnston, Rhode Island, USA) (Smith, 2009). Compressions of two micropillar geometries were simulated: tapered, with the micropillar geometry matching the one used in the actual experiments, and ideal, where the diameter of the micropillar was constant over its length. A displacement of 10% of the micropillar height was applied from the top. A part of the substrate below the micropillar was also included in the model to account for substrate deformation. The von Mises plasticity model was used with input values based on the experimental results from a former study (Kochetkova et al., 2021): Young's modulus was set to $E = 27.65$ GPa, yield stress was set to $\sigma_y = 0.318$ GPa, and the Poisson's ratio to $\nu = 0.3$. The effect of the taper on the elastic modulus, yield stress, and strain was expressed with the help of taper correction coefficients, representing the ratio of the apparent yield stress estimated for the ideal geometry divided by the one of the tapered micropillar geometry. Further details on the finite element simulations can be found in Appendix 2.

2.3. Morphological and compositional analysis

2.3.1. Micro-CT

Microscale computed tomography (micro-CT) scans of the samples were collected using microCT 100 (SCANCO Medical AG, Switzerland). Scanning was done at 55 kVp energy, 200 μA tube current, 400 × 2 ms integration time, and a voxel size of 6.6 μm. Micro-CT scanner was calibrated using hydroxyapatite phantoms with known density (−15, 100, 210, 415 and 790 mg/cm^3). Following the reconstruction, image processing was done using an in-house Matlab script. The sample scans were segmented with a fixed threshold of 711.11 mg/cm^3 (averaged value of each specimen-specific threshold, automatically detected by OTSU's method (Otsu, 1979)). For each sample average tissue mineral density (TMD) and bone volume ratio (BV/TV, bone volume vs. the total volume) were extracted. The main alignment of the sample pores was evaluated using an in-house Python script from an orthotropic fabric tensor with the mean surface length method as described by Hosseini et al. (2017). Consequently, the degree of anisotropy (DA) and the spatial orientation of the sample pores (out-of-plane angle) were calculated.

2.3.2. Raman spectroscopy

Raman spectra were acquired in ambient conditions using an upright Raman microscope (Nova Spectra, ND-MDT, Russia) equipped with a 633 nm laser. Spectra were collected through the 600 g/mm grid and 50 × objective with a numerical aperture of 0.75. The resultant laser spot size was ~0.5 μm in lateral and 1.6 μm in axial direction (Müller, 2006). The laser power at the sample surface was ~11 mW. For the whole-sample-level measurements, spectra were collected from interstitial ($N = 10$) and osteonal ($N = 10$) zones, as well as from plexiform zones ($N = 10$) for the Göttingen samples. Raman spectra give local information on the composition, and by uniformly distributing the measurement locations over the sample surface, global information per sample could be extracted. For each cortical bone zone, 10 spectra, 60 s integration time each, were collected approximately 5 μm underneath the bulk surface, resulting in 20–30 spectra per sample. Additionally, Raman measurements were carried out on the bone micropillars. An average of three spectra, 30s integration time each, were collected approximately 5 μm underneath the pillar top, providing the local information on the mineral to matrix ratio. Spectra processing was done in Python, detailed analysis steps with corresponding figures are shown in Appendix 3. All spectra where background-subtracted and peaks of interest representing mineral and collagen content were further analyzed. The ratio of the secondary phosphate (ν_2PO_4) over the amide III bands was used as an indirect estimation of the bone mineralization level (Roschger et al., 2014). Both peaks were fitted with a double Lorentzian function using a least-square scheme and the ratio of the integral areas provided the mineral to matrix ratio (Mineral/Matrix).

2.4. Statistical analysis

All statistical analysis was performed using R (R core team, R, 2021), rstatix package (Kassambara, 2021). The Shapiro-Wilk test was used to test for the normality of variables. Significant differences between paired datasets were then tested using the Wilcoxon rank-sum test to account for the non-normally distributed data (Oja, 2010), and the significance threshold was chosen as $p < 0.05$. Results for the normally distributed datasets are reported as mean ± SD, where SD stands for the standard deviation. Results for the non-normally distributed data are reported as median (IQR), where IQR stands for the interquartile range, i.e. the difference between the first and third quartile. Correlation analysis was done through linear regression analysis (lmtest package (Zeileis and Hothorn, 2002)).

3. Results

3.1. Whole sample level analysis

The visual analysis of the sample surfaces showed a discrepancy between observed zones of the cortical region. Similar to the human cortical bone morphology, osteonal and interstitial zones are observed on all three minipig genotypes (marked in Fig. 2 insets). Moreover, circumferential lamellae are observed on the outer side of the Yucatan and Sinclair samples. A large area of the plexiform bone is observed for all Göttingen minipigs, as marked in Fig. 2.

Micro-CT data showed that Göttingen minipigs had the highest tissue mineral density of 1229 ± 168 mg/cm^3 as well as the bone volume fraction of 98.1 ± 0.5%, while the Yucatan genotype demonstrated the lowest values: 1143 ± 163 mg/cm^3 and 96.3 ± 1.4%. Sinclair minipigs had a tissue mineral density of 1175 ± 161 mg/cm^3 and a bone volume fraction of 97.8 ± 0.7%. However, no significant difference between the genotypes was found for bone morphology, mineral density, and degree of anisotropy (Fig. 3). Moreover, the averaged out-of-plane orientation of the pores within the sample, including the Haversian canals, was 55° with 2° variation between the samples.

A significant difference ($p \leq 0.01$) was observed in the mineral to matrix ratio between all cortical bone zones within each of the three genotypes, except the osteonal and plexiform zones of Göttingen minipig. For all three genotypes, values were higher for interstitial zones than osteonal with the highest values for the Göttingen minipigs: 0.81 (0.13) for interstitial and 0.66 (0.12) for osteonal zones, although not significantly different from the Sinclair minipigs (Fig. 4). Yucatan genotype showed the lowest mineral to matrix ratio (0.74 (0.15) for interstitial and 0.57 (0.09) for osteonal zones), with a significant difference to the Göttingen minipigs for both zones. While this trend is similar to the mineral density data collected from micro-CT, a comparison between the two methods showed no significant correlation.

Indentation revealed higher elastic modulus and hardness for the interstitial zones of all genotypes compared to the osteonal and plexiform zones (Fig. 5). Göttingen and Sinclair samples showed a significant difference in elastic properties between the zones. Yucatan minipigs

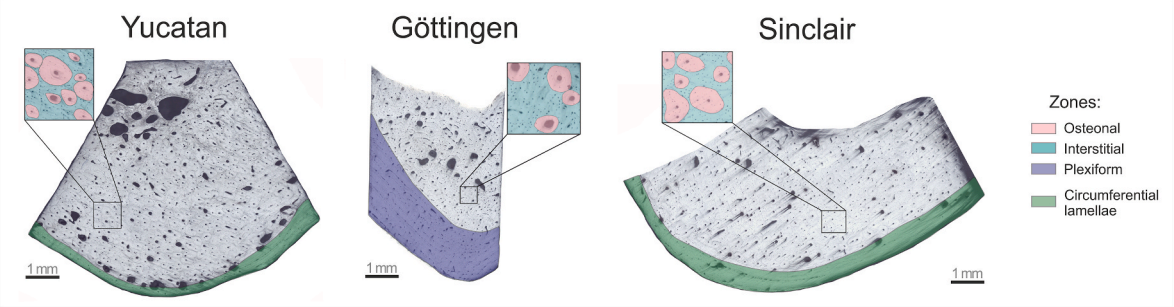

Fig. 2. Optical images of the representative samples' top surfaces of each genotype with the marked plexiform zone (indigo) and the circumferential lamellae (green), as well as the osteonal (rose-colored) and interstitial (aquamarine) zones marked in the insets.

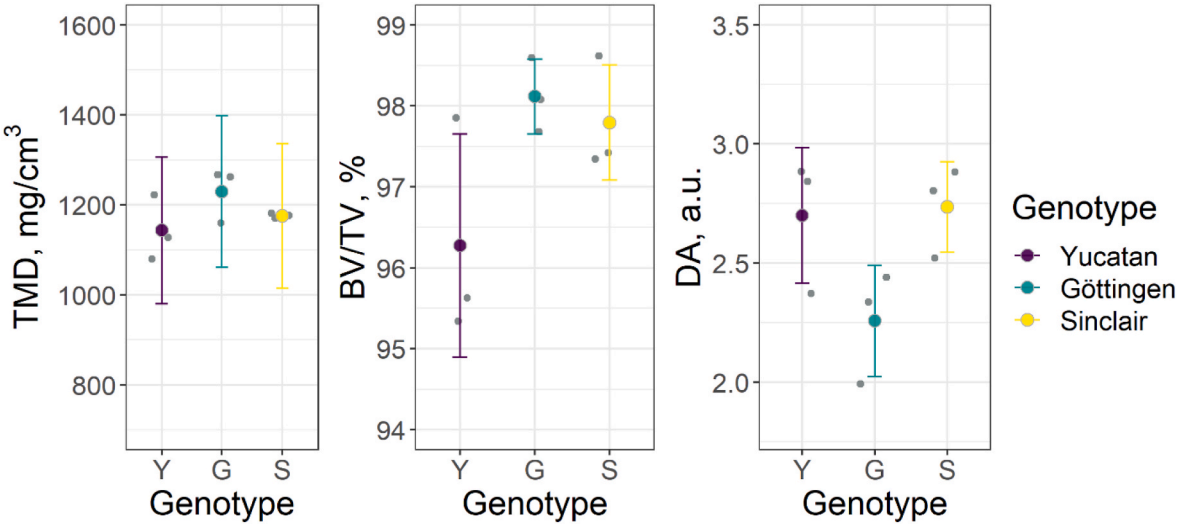

Fig. 3. Tissue Mineral Density (TMD), Bone Volume fraction (BV/TV), and Degree of Anisotropy of Haversian porosity (DA) of the cortical region of the jawbone of three minipigs genotypes.

exhibited the highest variation of the mean values within the zones, however, the hardness was still significantly different between the interstitial and the osteonal zones.

Correlation analysis was performed to check the dependence between the average bone elastic properties measured via nanoindentation and average bone mineralization, as assessed through two techniques: micro-CT (TMD) and Raman spectroscopy (Mineral/Matrix ratio). No significant dependence was observed between the tissue mineral density and both elastic modulus and hardness. Moreover, no correlation was detected between the elastic modulus and the mineral to matrix ratio, while a significant positive trend was found between the hardness and the mineral to matrix ratio for pooled cortical bone zones (Fig. 6).

3.2. Site-matched micropillar compression and Raman spectroscopy

At the microscale level, significantly different mineralization was observed between the three genotypes, as assessed via the mineral to matrix Raman band ratio (Fig. 7). Göttingen and Yucatan genotypes exhibit the highest and the lowest mineral/matrix ratio accordingly. Observed alterations of bone mineralization at the microscale match the mineral/matrix ratio variations at the whole sample level (Fig. 4).

Micropillar compression revealed the highest mean value of the Young's modulus for the Sinclair minipigs, although only the difference with the Yucatan minipigs was significant due to the scatter of the Young's modulus data of the Sinclair minipigs. No significant difference was observed between the Young's modulus mean values of the Yucatan and Göttingen genotypes. The mean yield stress values follow the genotype mineralization, with the Göttingen and Yucatan minipigs demonstrating the highest and the lowest values, respectively. However, the yield strain mean values were not significantly different between the Göttingen and Sinclair genotypes, but both were significantly lower than the ones of the Yucatan ($p \leq 0.0001$).

Site-matched micropillar compression and Raman spectra collection allowed us to assess the relationship between the genotype relative mineralization and the local mechanical properties. The correlative analysis showed no significant dependence between the local elastic and the yield properties versus the mineral to matrix ratio (Fig. 8).

Three distinct micropillar failure modes were observed after compression. Axial cracking, where the fracture followed the main micropillar axis (Fig. 9 A), was the most common mode followed by shear (Fig. 9 C) and mushrooming (Fig. 9 B), where the major deformation occurred at the micropillar top. The correlative analysis showed no dependence between the failure modes and the mechanical properties or relative mineralization.

4. Discussion

This study presented the framework for the multimodal characterization of the jawbone in an animal model that could be further extended to humans. It is the first report on the jawbone properties at the microscale level for the three minipig genotypes: Yucatan, Göttingen, and Sinclair, all commonly used in dental research due to their anatomical similarity to humans.

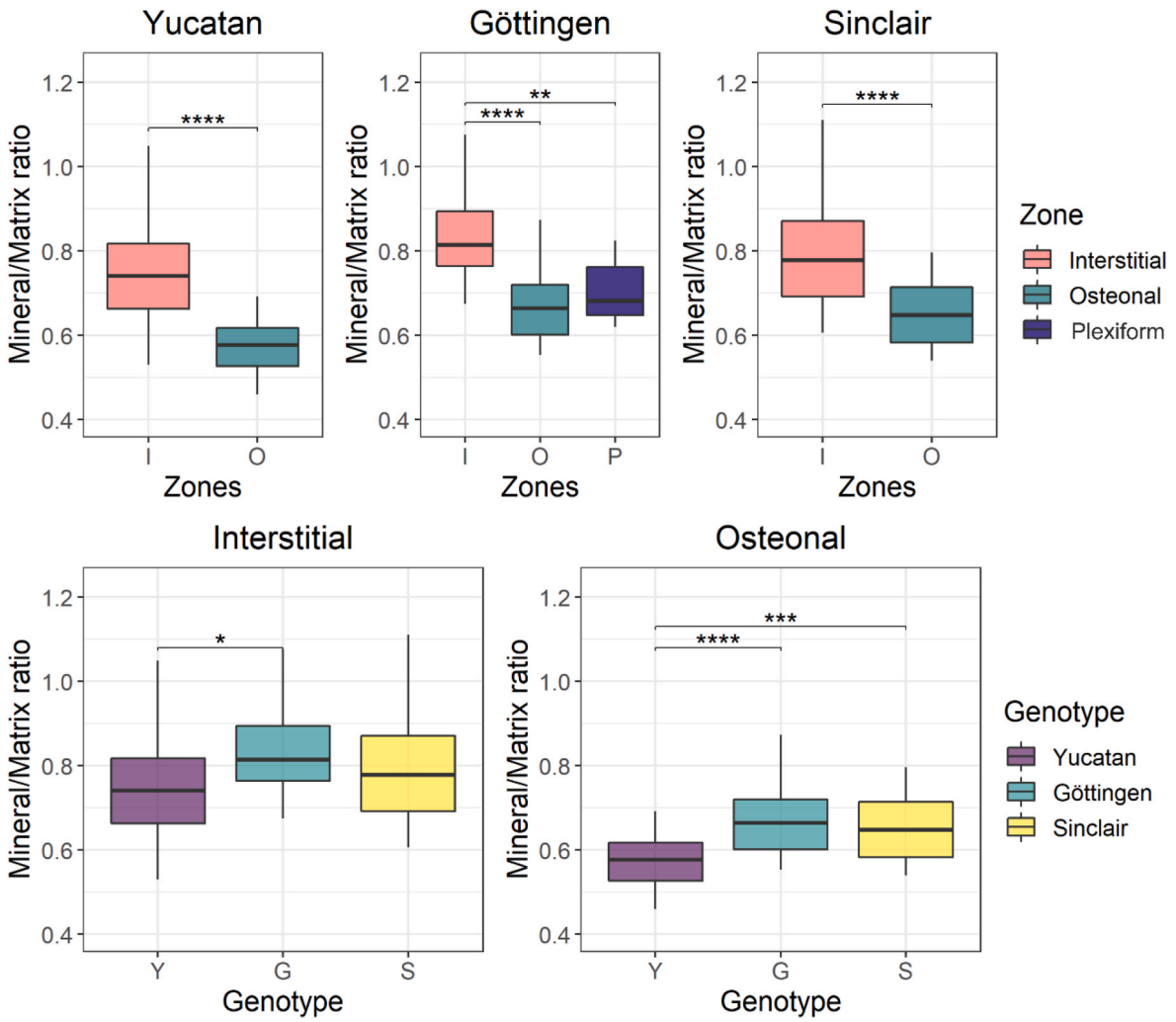

Fig. 4. Mineral to matrix ratios as estimated at interstitial, osteonal, and plexiform zones of three minipigs genotypes. Statistical significance asterisks: * − $p \leq 0.05$, ** − $p \leq 0.01$, *** − $p \leq 0.001$, **** − $p \leq 0.0001$.

4.1. Whole sample level analysis

At the whole sample level measurements, the micro-CT technique was used to shed light on potential differences between the genotypes both in mineralization and bone volume fraction. No statistically significant differences were observed between the genotypes, most likely due to the very low pore volume fraction and variation in zonal properties within the samples. Testing a larger number of regions of interest per mandibular bone would improve the comparison between the genotype. It is of high interest to investigate several sections within each mandibular in the future, to account for the inherent variations of compositional and, consequently, mechanical properties within the whole bone volume. Surprisingly, tissue mineral density, extracted from the micro-CT, did not correlate with the Raman mineral to matrix ratio as reported in the study of Indermaur et al. (2021), which might be rationalized by the relatively low number of samples (N = 3 per genotype) together with the small range of mineral to matrix ratio.

Since the jawbone has irregular morphology with highly-porous alveolar and dense compact bone regions, the available data on the jawbone mineralization could not be compared to the measurements on the compact mandibular bone from the current study. However, investigated bone regions exhibited clear zonal morphology with low porosity, similar to that of other types of human cortical bone. Indeed, the Raman mineral to matrix ratio of examined minipig jaws was within the range of the reported values for the human femoral midshafts: 0.57–0.81 for the minipig jaws examined in the current study and 0.3–1.5 for the human femur (Roschger et al., 2014). Moreover, the TMD values of investigated minipig jaws were at the lower border of the reported TMD range for the human femoral cortex, measured at a similar voxel size: 1128–1260 mg/cm^3 for the minipigs and 1200–1600 mg/cm^3 for the human femur (Deuerling et al., 2010). Since only the cortical part from the inferior jawbone border was examined, the bone volume fraction was high for all tested minipigs jaws samples, with only 2–4% porosity. These values are close to those of the other animal species (5–6%) (Martin and Boardman, 1993; Sietsema, 1995; Iezzi et al., 2020).

A clear difference between the interstitial and osteonal zones was visible for both Raman and nanoindentation measurements. This is similar to what is usually observed in the cortical parts of other skeletal bones, with the interstitial zone exhibiting higher mineralization and hardness (Nyman et al., 2011; Zysset et al., 1999). Interestingly, a significant difference between the genotypes was more pronounced between the osteonal regions of cortical bone. This might be a result of constant jawbone turnover, during which the interstitial zones rapidly reach the saturated mineralization levels (Hesse et al., 2015), which are comparable between the three genotypes.

An increase in mineral to matrix ratio accounted for the jawbone hardness increase but no dependence was observed for the elastic moduli. Since elastic modulus is more sensitive to the alterations in the underlying sample morphology, other factors like structural anisotropy and microporosity may have a comparable influence on the elastic

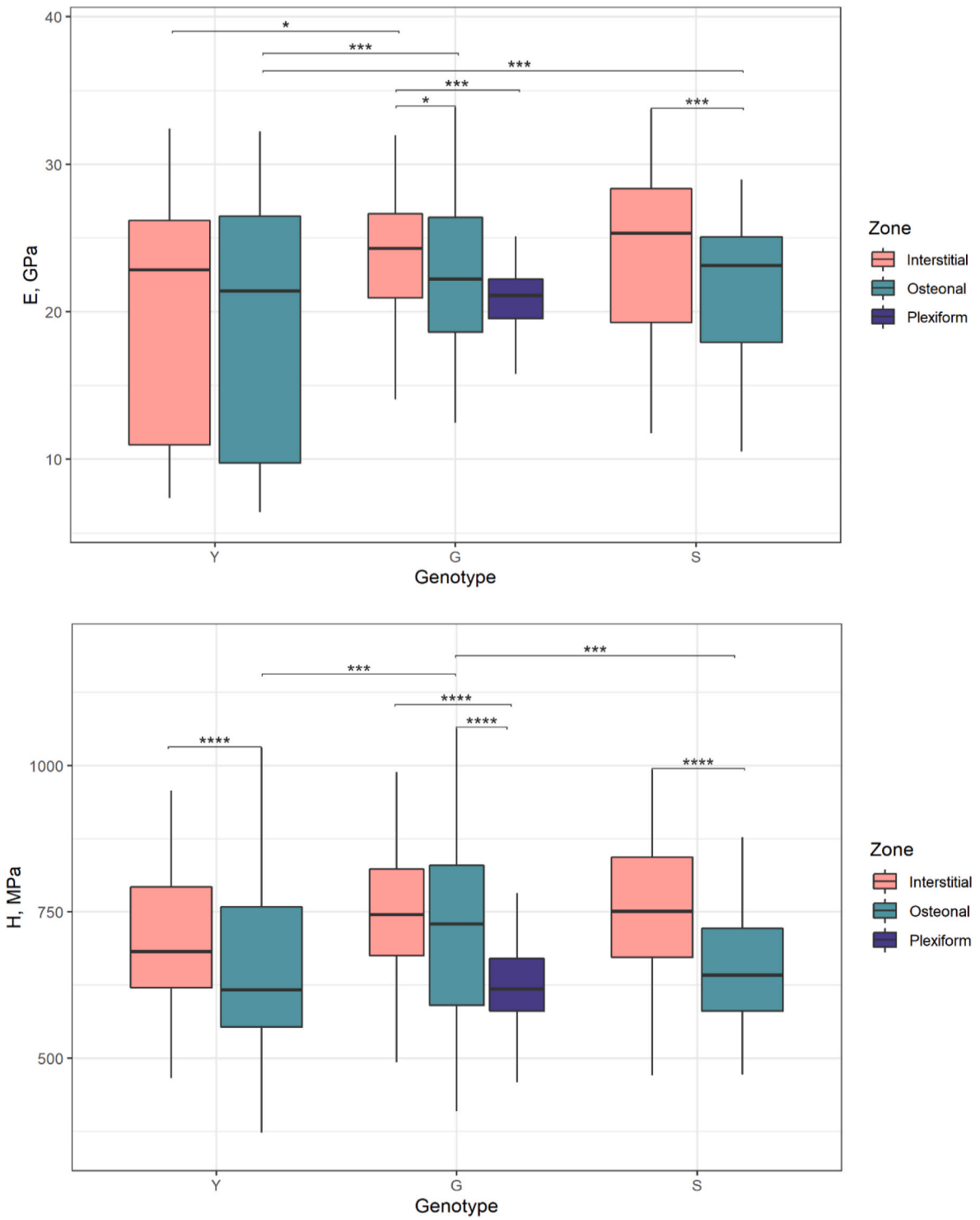

Fig. 5. Young modulus (E) and hardness (H) as estimated at interstitial, osteonal, and plexiform zones of three minipig genotypes: Yucatan, Göttingen, Sinclair. Statistical significance asterisks: * − $p \leq 0.05$, ** − $p \leq 0.01$, *** − $p \leq 0.001$, **** − $p \leq 0.0001$.

properties thereby concealing a possible correlation with mineral to matrix ratio. Moreover, the large variations of the elastic modulus values within the Yucatan genotype might have faded the possible correlation between the elastic modulus and the relative mineralization.

4.2. Site-matched micropillar compression and Raman spectroscopy

To date, microscale compression experiments on bone were solely performed on focused ion beam (FIB) milled micropillars (Schwiedrzik et al., 2014, 2017; Indermaur et al., 2021; Groetsch et al., 2019; Kochetkova et al., 2021; Peruzzi et al., 2021) In the current study, bone micropillars were fabricated using ultrashort pulsed laser ablation, drastically decreasing the time costs for micromachining and simultaneously enabling high throughput analysis. However, we had to compromise the output micropillar geometry: the micropillars were approximately 5 times bigger in comparison to previous studies on micropillar compression. Moreover, laser-fabricated micropillars had a taper, which affected the stress distribution and hence also the measured

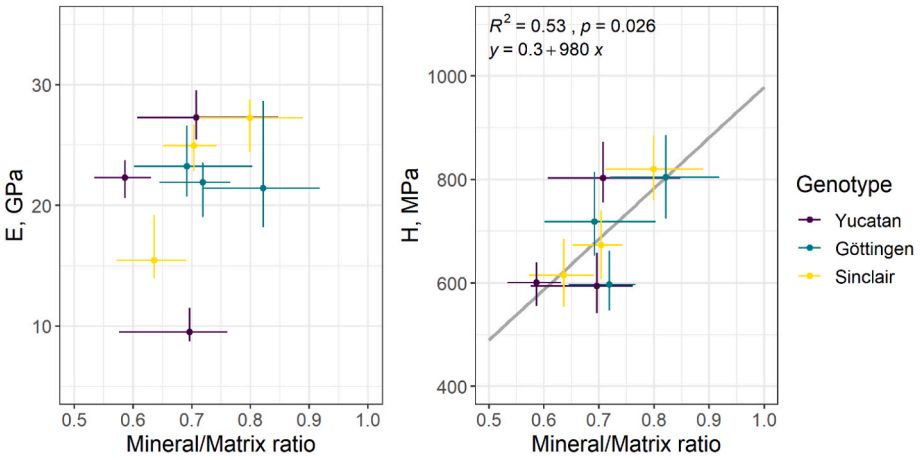

Fig. 6. Bone Young modulus (E) and hardness (H) versus bone mineral to matrix ratio.

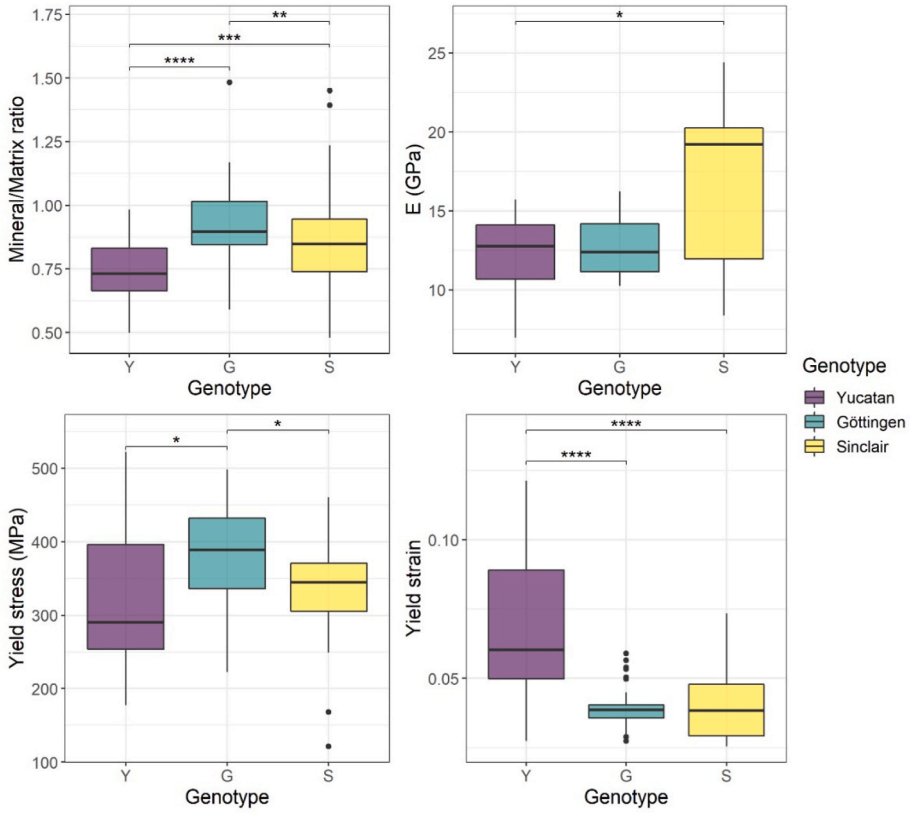

Fig. 7. Microscale bone properties of three minipigs genotypes. Statistical significance asterisks: * − p ≤ 0.05, ** − p ≤ 0.01, *** − p ≤ 0.001, **** − p ≤ 0.0001.

apparent yield point of the compression experiments. A possible remedy for the pillar taper would be additional FIB milling atop a fabricated pillar, similarly to the study of Groetsch et al. (2019), however, this approach would be still time-consuming (~1h per pillar). We, therefore, kept the laser-ablated micropillars with geometrical flaws and accounted for the deviation from the ideal cylindrical shape by finite-element simulations. This way we were able to keep the high throughput of microscale compression experiments, meanwhile correcting the output mechanical properties for the micropillar taper. Since laser ablation was done at the normal atmospheric pressure and relative humidity, we reduced the crack formation at the sample surface, which is commonly observed after high vacuum exposure during FIB milling. Another advantage of the laser-ablated micropillars is the possibility to carry the site-matched Raman spectra collection. This was not possible earlier with the FIB milled micropillars due to inevitable sample sputtering with a conductive metal, which hinders the Raman signal.

From the micropillar measurements, we were able to detect significant differences between the genotypes' mineralization and yield properties. While local measurements of relative mineralization followed those at the global level, the differences between genotypes were more pronounced at the local level. Surprisingly, neither elastic nor yield mechanical properties of jawbone micropillars showed a correlation with the bone relative mineralization. Such correlation was previously observed by Indermaur et al. (2021) in human transilliac osteonal bone. However, the micropillars dimensions used in the current study were five times bigger and thus contained a higher number of lacunae

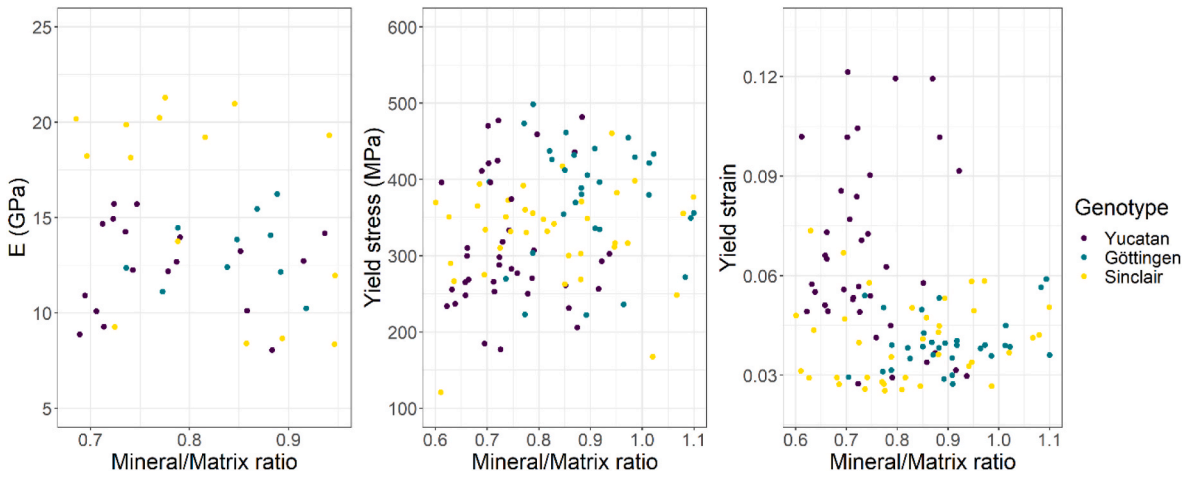

Fig. 8. Elastic modulus and yield properties versus the mineral to matrix ratio as assessed for three minipig genotypes.

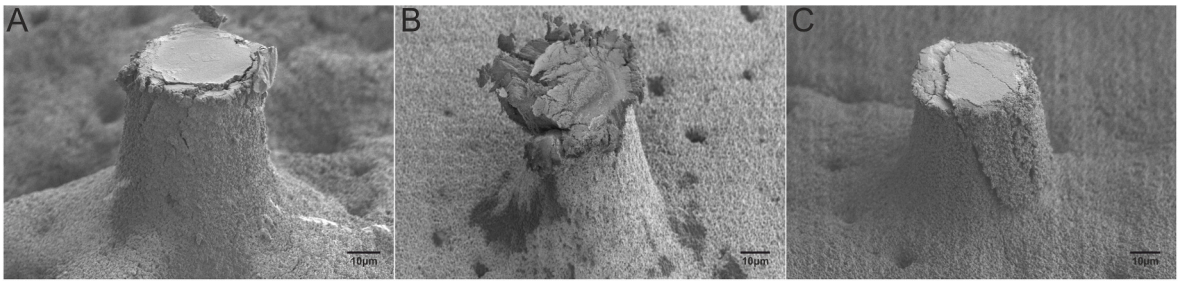

Fig. 9. Observed fracture modes of compressed micropillars. A – axial cracking, B – mushrooming, C – shear.

inclusions and lamellar interfaces. As was shown by Casari et al. (2021), the increase in the size of the microscale specimen leads to lower strength rationalized by the higher probability of finding flaws in a critical orientation. The dominant failure mode of micropillars in our study was axial cracking. As was demonstrated in other studies on micropillar compression of the ovine and bovine bone (Kochetkova et al., 2021; Peruzzi et al., 2021), such failure mode is most likely driven by the axial alignment of the mineralized collagen fibrils.

Overall, we observe large variations of mechanical properties within the minipig genotypes, both for the nanoindentation and micropillar compression measurements. This is likely caused by the inherent structural variations at different locations in the jaw as well as between the animals of the same genotype. Besides, the mineralized collagen fibrils orientation within the tested local volumes was assumed to match the overall orientation of Haversian canals within the sample volume. For future experiments, the quantitative polarized Raman method can be applied for the simultaneous mineralized collagen fibrils orientation estimation and compositional characterization (Kochetkova et al., 2021).

4.3. Study limitations

The current study was carried out on the premolar region of the mandible, opposite to the teeth growth. It is, however, of high interest to investigate the alveolar bone, due to its relevant location for implant placement and other dental manipulations. The samples used in the current work were collected after the completion of other dental studies, for which the alveolar bone was already extracted. Yet, we hypothesize that the mandibular part of the jaw opposite to the teeth growth may be of interest for future studies using CT imaging because it is not affected by the intensity of artifacts coming from metallic implants, crowns, or fillings (Vitulli et al., 2022; Lofthag-Hansen et al., 2007). Nevertheless, the proposed framework for the bone quality assessment can be applied to the alveolar region of bone in the future.

All samples were stored in formalin before any preparation steps. It is accepted that fresh bones represent the *in vivo* conditions better than formalin-fixed ones. Nevertheless, formalin-fixed specimens are frequently used in biomechanical testing due to the lack of fresh bones. Chemical fixation with formalin affects the organic fraction of the bone, in particular, the collagen cross-links (Chapman et al., 1990; Currey et al., 1995). In the current study, we abstain from any direct analysis of the organic bone components, but future analysis of the fresh bone samples following the proposed framework can be done through Raman spectroscopy. As was shown in the study of K. J. Burkhart et al., formalin-fixed human diaphyseal bone exhibit higher stiffness (about 14% after 6 weeks of conservation) but no differences in bone mineral density values (Burkhart et al., 2010). Similarly, S.J. Edmondston and colleagues stated that formalin fixation may result in a slight increase in compressive strength but this does not appear to be associated with a systematic change in mineral density (Edmondston et al., 1994). Considering that earlier reported mechanical experiments were performed at the macroscale, we expect a higher effect of formalin fixation at the microscale mechanical properties of mandibular bone. However, the sample storage and preparation steps were consistent between the samples of all genotypes, allowing us to detect the differences between the inherent genotypes' properties.

5. Conclusion

We report the jawbone's mechanical and morphological properties together with relative mineralization at the microscale. Three minipig genotypes were examined: Yucatan, Göttingen, and Sinclair, all commonly used in preclinical dental research. Raman spectroscopy proved to be a perspective method for relative mineralization estimation, highlighting the differences between the mineral to matrix ratios of the minipig genotypes. A novel laser-ablation protocol for micropillar fabrication allowed a high throughput analysis of the microscale compressive properties of the jawbone. Site-matched micropillar

compression and Raman spectroscopy then gave access to the bone structure-property relationships. Observed variations in the output mechanical parameters, both at the local and averaged global levels, may be attributed to the structural and compositional heterogeneity of the samples. Measuring local compositional and mechanical properties in a site-matched fashion can shed light on structure-property relationships of bone at the microscale. However, to extend the analysis, mineralized collagen fibril orientation and structural defects like hidden osteocytes and microvascular channels need to be taken into account explicitly in the future. Overall, the methods used at the whole sample level could be potentially correlated to the medical tools used to assess jawbone toughness and morphology in clinics. At the same time, the site-matched characterization methods can be applied to specify the local mechanical and mineralization properties of the jawbone.

CRediT authorship contribution statement

Tatiana Kochetkova: Writing – review & editing, Writing – original draft, Visualization, Project administration, Methodology, Investigation, Formal analysis, Data curation, Conceptualization. **Alexander Groetsch:** Writing – review & editing, Methodology, Investigation, Formal analysis, Data curation. **Michael Indermaur:** Writing – review & editing, Investigation, Formal analysis, Data curation. **Cinzia Peruzzi:** Writing – review & editing, Visualization, Formal analysis, Data curation. **Stefan Remund:** Writing – review & editing, Methodology. **Beat Neuenschwander:** Writing – review & editing, Methodology. **Benjamin Bellon:** Resources, Conceptualization, Writing - review & editing. **Johann Michler:** Funding acquisition, Resources. **Philippe Zysset:** Writing – review & editing, Supervision, Conceptualization. **Jakob Schwiedrzik:** Writing – review & editing, Supervision, Resources, Funding acquisition, Conceptualization.

Declaration of competing interest

The authors declare that they have no known competing financial interests or personal relationships that could have appeared to influence the work reported in this paper.

Data availability

Data will be made available on request.

Acknowledgments

This work is funded by the Special Focus Area Personalized Health and Related Technologies (SFA PHRT) iDoc Project 2017–304 (TK) and Swiss National Science Foundation (SNSF) Ambizione grant no. 174192 (CP and JS) and SNSF grant no. 165510 (MI). The authors would like to thank J. Hofstetter, B. Pippenger and R. Wagner for the helpful discussions, and P. Bühlmann for statistical advice.

Appendix 1. Estimated heat accumulation during laser ablation

Accumulated heat during laser ablation was estimated following the work of R. Weber et al., 2014, 2017. For the unidirectional scanning mode, the finite number of subsequent pulses on the same spot causes heat accumulation. The temperature fields of each pulse can be summed up in time and space when the material parameters are taken as constant. Solving the heat conduction equation for the 3D heat flow leads to the temperature field shown in eq. (A1), where the heat residual Q_{3D} define the heat which is released in an infinitely short time at t = 0.

$$\Delta T(t) = \frac{Q_{3D}}{\rho \cdot c_p \cdot \sqrt{\left(\frac{4\pi \cdot \kappa}{f_r}\right)^3}} \cdot b_{3D}, \quad where \;\; b_{3D} = \frac{-2}{\sqrt{t \cdot f_r}} + 2.61. \tag{A1}$$

The input values used for the calculations are summed up in Table A1. The bone tissue parameters were taken from S. McPhee and A. Groetsch et al. (McPhee et al., 2021).

Table A1
Laser ablation and bone tissue parameters used for the heat accumulation calculations.

P_{av} =	0.012	W	Average laser power
f_{rep} =	3	kHz	Repetition rate
E_p =	4	μJ	Pulse energy
w_0 =	7	μm	Spot radius
R =	0.4		Surface reflectivity
η =	0.5		Absorbed part converted to heat
v_{mark} =	15	mm/s	Laser scanning speed
p_x =	5	μm	Distance between 2 pulses
n_p =	3		Number of pulses at the same position*
t =	0.001	s	Time for n_p Pulses
ρ =	2033	kg/m^3	Density
c_p =	1440	J/kg/K	Specific heat
k =	0.54	W/m/K	Thermal conductivity
κ =	1.8E-07	m^2/s	Thermal diffusivity

* - The number of pulses is calculated by dividing the beam diameter by the distance between 2 pulses.

As a result, residual heat is estimated to be $Q_{3D} = 2.4\mu J$ and the maximum temperature increase $\Delta T = 55.6°C$. This temperature is about 10 °C below the denaturation point of native hydrated collagen, and 100 °C below the denaturation point of dehydrated mineralized collagen (Bozec and Odlyha, 2011). Since the period between two consecutive laser ablations at the same spot exceeds 2 min, there is no additional heat accumulation between the consecutive ablation layers. Moreover, these calculations were carried out with several assumptions: (i) energy input is taken as the point source with instantaneous stationary energy, (ii) surface instead of volume absorption, and (iii) the surface is assumed to be fully isolated. These simplifications lead to overestimated heat accumulation. We assume that the real heat accumulations during ablation are below the calculated ones.

It is important to mention that we used simplified estimations of the pulse to pulse heat accumulations, as the heating from the pulse itself on a short timescale was not discussed. This aspect would require additional, more time expensive simulations following the two temperature model as proposed by S. McPhee and A. Groetsch et al. (McPhee et al., 2021).

Appendix 2. FE simulations of micropillar taper effect on the output mechanical properties

We determined the effects of the micropillars' taper on the elastic modulus, yield stress, and strain by means of finite element (FE) simulations. The average dimensions of the nine samples (25 micropillars per sample) were determined by HRSEM (Hitachi S4800, Japan). These average dimensions were used to model the micropillars with and without taper in Abaqus/CAE (Dassault Systemes Simulia Corp., Johnston, Rhode Island, USA). For the micropillars without taper, the bottom diameter was set equal to the top diameter. The substrate below the micropillar was also included in the model to account for substrate compliance. A displacement of 10% of the micropillar height was applied, which is equal to 10% strain. Young's modulus was set to E = 27.65 GPa and Poisson's ratio to $\nu = 0.3$. The standard von Mises plasticity model was used and the yield stress was set to $\sigma_y = 0.318$ GPa. The Young's modulus and the yield stress are based on experimental results from a former study (Kochetkova et al., 2021). Hexahedral elements (C3D8) were used to mesh the model and a mesh sensitivity analysis was conducted. The mesh convergence was achieved when reducing the size of the elements by half resulted in a change in yield stress of less than 0.1%. The effect of the taper on the elastic modulus, the yield stress and strain are represented as

$$k_E = \frac{E_{ideal}}{E_{tapered}}, \quad k_\sigma = \frac{\sigma_{ideal}}{\sigma_{tapered}}, \quad k_\xi = \frac{\xi_{ideal}}{\xi_{tapered}}.$$

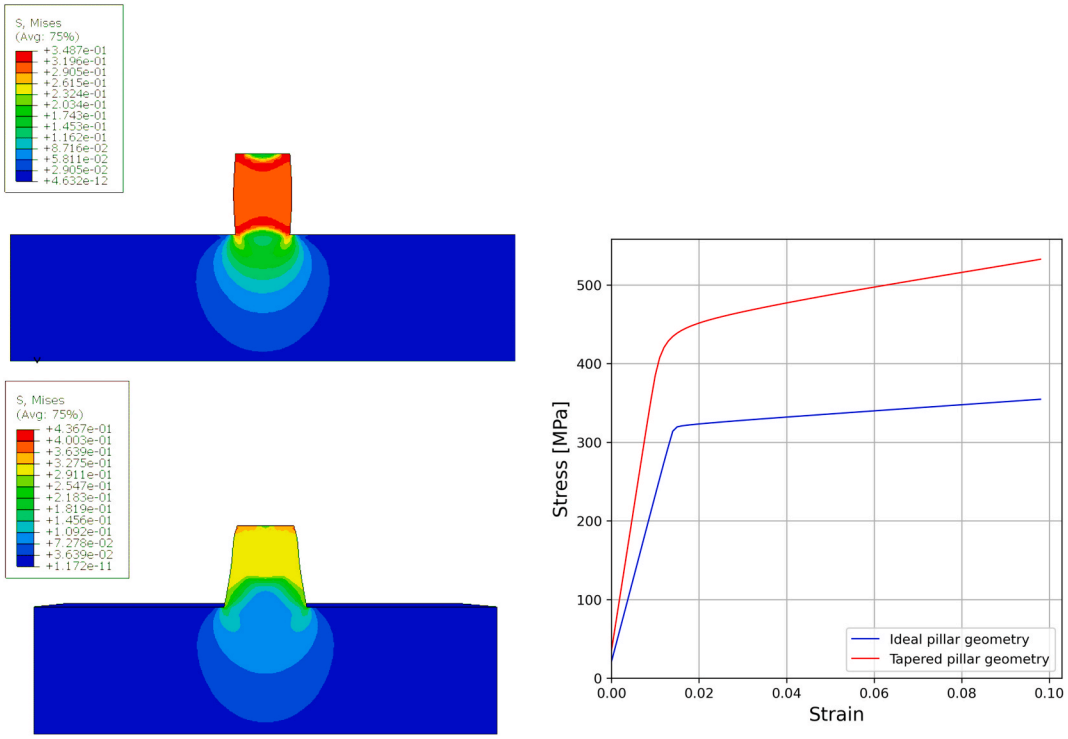

Fig. A2. Distribution of von Mises stresses during compression simulations for micropillars with ideal (top) and tapered (bottom) geometries and corresponding stress-strain curves.

Appendix 3. Raman spectra processing

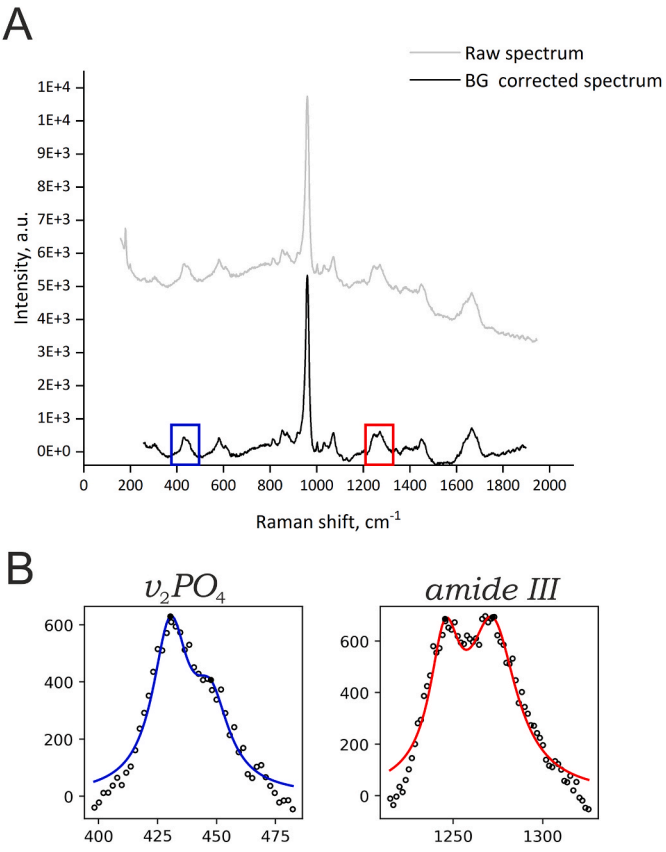

Fig. A3. *Raman spectra processing steps for the raw data using Python software* (van Rossum and Drake, 2009):
(A) Background (BG) subtraction for the whole spectra (second-order polynomial fit for local minima, numpy.polyfit).
(B) v_2PO_4 and amide III band analysis:
• additional linear BG subtraction (first order polynomial fit for local minima on both sides of the band, numpy.polyfit);
• *double-Lorentzian fit of v_2PO_4 (blue) and amide III (red); extracting peak integral areas: 410*-460 cm^{-1} *for v_2PO_4 and 1215*-1300 cm^{-1} *for amide III* (Roschger et al., 2014).

References

Alsaadi, G., Quirynen, M., Michiels, K., Jacobs, R., van Steenberghe, D., 2007. A biomechanical assessment of the relation between the oral implant stability at insertion and subjective bone quality assessment. J. Clin. Periodontol. 34, 359–366. https://doi.org/10.1111/j.1600-051X.2007.01047.x.

An, Y.H., Friedman, R.J., 2020. In: Animal Models in Orthopaedic Research. CRC Press. https://doi.org/10.1201/9780429173479.

Angker, L., Swain, M.V., 2006. Nanoindentation: application to dental hard tissue investigations. J. Mater. Res. 21, 1893–1905. https://doi.org/10.1557/jmr.2006.0257.

P. Aranyarachkul, J. Caruso, B. Gantes, E. Schulz, M. Riggs, I. Dus, J.M. Yamada, M. Crigger, Bone density assessments of dental implant sites: 2. Quantitative cone-beam computerized tomography., Int. J. Oral Maxillofac. Implants. 20 (n.d.) 416–424.

Baumgaertel, S., Palomo, J.M., Palomo, L., Hans, M.G., 2009. Reliability and accuracy of cone-beam computed tomography dental measurements. Am. J. Orthod. Dentofacial Orthop. 136, 19–25. https://doi.org/10.1016/j.ajodo.2007.09.016.

Bozec, L., Odlyha, M., 2011. Thermal denaturation studies of collagen by microthermal analysis and atomic force microscopy. Biophys. J. 101, 228–236. https://doi.org/10.1016/j.bpj.2011.04.033.

Burkhart, K.J., Nowak, T.E., Blum, J., Kuhn, S., Welker, M., Sternstein, W., Mueller, L.P., Rommens, P.M., 2010. Influence of formalin fixation on the biomechanical properties of human diaphyseal bone. Biomedizinische Technik/Biomedical Engineering 55, 361–365. https://doi.org/10.1515/bmt.2010.043.

Buser, D., Schenk, R.K., Steinemann, S., Fiorellini, J.P., Fox, C.H., Stich, H., 1991. Influence of surface characteristics on bone integration of titanium implants. A histomorphometric study in miniature pigs. J. Biomed. Mater. Res. 25, 889–902. https://doi.org/10.1002/jbm.820250708.

Casari, D., Kochetkova, T., Michler, J., Zysset, P., Schwiedrzik, J., 2021. Microtensile failure mechanisms in lamellar bone: influence of fibrillar orientation, specimen size and hydration. Acta Biomater. 131, 391–402. https://doi.org/10.1016/j.actbio.2021.06.032.

Chapman, J.A., Tzaphlidou, M., Meek, K.M., Kadler, K.E., 1990. The collagen fibril—a model system for studying the staining and fixation of a protein. Electron. Microsc. Rev. 3, 143–182. https://doi.org/10.1016/0892-0354(90)90018-N.

Compston, J., 2006. Bone quality: what is it and how is it measured? Arq. Bras. Endocrinol. Metabol. 50, 579–585. https://doi.org/10.1590/S0004-27302006000400003.

Currey, J.D., Brear, K., Zioupos, P., Reilly, G.C., 1995. Effect of formaldehyde fixation on some mechanical properties of bovine bone. Biomaterials 16, 1267–1271. https://doi.org/10.1016/0142-9612(95)98135-2.

Deuerling, J.M., Rudy, D.J., Niebur, G.L., Roeder, R.K., 2010. Improved accuracy of cortical bone mineralization measured by polychromatic microcomputed tomography using a novel high mineral density composite calibration phantom. Med. Phys. 37, 5138–5145. https://doi.org/10.1118/1.3480507.

Edmondston, S.J., Singer, K.P., Day, R.E., Breidahl, P.D., Price, R.I., 1994. Formalin fixation effects on vertebral bone density and failure mechanics: an in-vitro study of human and sheep vertebrae. Clin. BioMech. 9, 175–179. https://doi.org/10.1016/0268-0033(94)90018-3.

Feldkamp, L.A., Goldstein, S.A., Parfitt, M.A., Jesion, G., Kleerekoper, M., 2009. The direct examination of three-dimensional bone architecture in vitro by computed tomography. J. Bone Miner. Res. 4, 3–11. https://doi.org/10.1002/jbmr.5650040103.

M.Á. Fuster-Torres, M. Peñarrocha-Diago, D. Peñarrocha-Oltra, M. Peñarrocha-Diago, Relationships between bone density values from cone beam computed tomography, maximum insertion torque, and resonance frequency analysis at implant placement: a pilot study., Int. J. Oral Maxillofac. Implants. 26 (n.d.) 1051–1056.

Graham, J., 2015. Detecting low bone mineral density from dental radiographs: a mini-review. Clin. Cases Miner. Bone Metabol. 12, 178–182. https://doi.org/10.11138/ccmbm/2015.12.2.178.

Groetsch, A., Gourrier, A., Schwiedrzik, J., Sztucki, M., Beck, R.J., Shephard, J.D., Michler, J., Zysset, P.K., Wolfram, U., 2019. Compressive behaviour of uniaxially aligned individual mineralised collagen fibres at the micro- and nanoscale. Acta Biomater. https://doi.org/10.1016/j.actbio.2019.02.053.

Groetsch, A., Zysset, P.K., Varga, P., Pacureanu, A., Peyrin, F., Wolfram, U., 2021. An experimentally informed statistical elasto-plastic mineralised collagen fibre model at the micrometre and nanometre lengthscale. Sci. Rep. 11 https://doi.org/10.1038/S41598-021-93505-0.

Hau, J., 2008. Animal models for human diseases. In: Sourcebook of Models for Biomedical Research. Humana Press, Totowa, NJ. https://doi.org/10.1007/978-1-59745-285-4_1.

Hesse, B., Varga, P., Langer, M., Pacureanu, A., Schrof, S., Männicke, N., Suhonen, H., Maurer, P., Cloetens, P., Peyrin, F., Raum, K., 2015. Canalicular network morphology is the major determinant of the spatial distribution of mass density in human bone tissue: evidence by means of synchrotron radiation phase-contrast nano-CT. J. Bone Miner. Res. 30, 346–356. https://doi.org/10.1002/JBMR.2324.

Hosseini, H.S., Maquer, G., Zysset, P.K., 2017. μCT-based trabecular anisotropy can be reproducibly computed from HR-pQCT scans using the triangulated bone surface. Bone 97, 114–120. https://doi.org/10.1016/j.bone.2017.01.016.

Hua, Y., Nackaerts, O., Duyck, J., Maes, F., Jacobs, R., 2009. Bone quality assessment based on cone beam computed tomography imaging. Clin. Oral Implants Res. 20, 767–771. https://doi.org/10.1111/j.1600-0501.2008.01677.x.

Iezzi, G., Mangano, C., Barone, A., Tirone, F., Baggi, L., Tromba, G., Piattelli, A., Giuliani, A., 2020. Jawbone remodeling: a conceptual study based on Synchrotron High-resolution Tomography. Sci. Rep. 10 https://doi.org/10.1038/S41598-020-60718-8.

Imwinkelried, T., Beck, S., Schaller, B., 2020. Pre-clinical testing of human size magnesium implants in miniature pigs: implant degradation and bone fracture healing at multiple implantation sites. Mater. Sci. Eng. C 108, 110389. https://doi.org/10.1016/j.msec.2019.110389.

Indermaur, M., Casari, D., Kochetkova, T., Peruzzi, C., Zimmermann, E., Rauch, F., Willie, B., Michler, J., Schwiedrzik, J., Zysset, P., 2021. Compressive strength of iliac bone ECM is not reduced in osteogenesis imperfecta and increases with mineralization. J. Bone Miner. Res. 36, 1364–1375. https://doi.org/10.1002/jbmr.4286.

Jacobs, R., Salmon, B., Codari, M., Hassan, B., Bornstein, M.M., 2018. Cone beam computed tomography in implant dentistry: recommendations for clinical use. BMC Oral Health 18, 88. https://doi.org/10.1186/s12903-018-0523-5.

Kassambara, Alboukadel, 2021. Rstatix: Pipe-Friendly Framework for Basic Statistical Tests.

Kobayashi, E., Hishikawa, S., Teratani, T., Lefor, A.T., 2012. The pig as a model for translational research: overview of porcine animal models at Jichi Medical University. Transplant. Res. 1, 8. https://doi.org/10.1186/2047-1440-1-8.

Kochetkova, T., Peruzzi, C., Braun, O., Overbeck, J., Maurya, A.K., Neels, A., Calame, M., Michler, J., Zysset, P., Schwiedrzik, J., 2021. Combining polarized Raman spectroscopy and micropillar compression to study microscale structure-property relationships in mineralized tissues. Acta Biomater. 119, 390–404. https://doi.org/10.1016/j.actbio.2020.10.034.

Kuhn, J.L., Goldstein, S.A., Feldkamp, L.A., Goulet, R.W., Jesion, G., 1990. Evaluation of a microcomputed tomography system to study trabecular bone structure. J. Orthop. Res. 8, 833–842. https://doi.org/10.1002/jor.1100080608.

Kuo, T.-F., Lu, H.-C., Tseng, C.-F., Yang, J.-C., Wang, S.-F., Yang, T.C.-K., Lee, S.-Y., 2017. Evaluation of osseointegration in titanium and zirconia-based dental implants with surface modification in a miniature pig model. J. Med. Biol. Eng. 37, 313–320. https://doi.org/10.1007/s40846-017-0230-8.

S. Lee, B. Gantes, M. Riggs, M. Crigger, Bone density assessments of dental implant sites: 3. Bone quality evaluation during osteotomy and implant placement., Int. J. Oral Maxillofac. Implants. 22 (n.d) 208–212.

Lekholm, G.A., Zarb, U., 1985. Patient selection and preparation. In: Brånemark, T., P, I., Zarb, G., Albrektsson (Eds.), Tissue Integrated Prosthesis: Osseointegration in Clinical Dentistry. Quintessence publishing Co. Inc., Chicago, p. 199.

Leroy, G., Penel, G., Leroy, N., Brès, E., 2002. Human tooth enamel: a Raman polarized approach. Appl. Spectrosc. 56, 1030–1034. https://doi.org/10.1366/000370202760249765.

Lim, Y.C., Altman, K.J., Farson, D.F., Flores, K.M., 2009. Micropillar fabrication on bovine cortical bone by direct-write femtosecond laser ablation. J. Biomed. Opt. 14, 064021 https://doi.org/10.1117/1.3268444.

Litten-Brown, J.C., Corson, A.M., Clarke, L., 2010. Porcine models for the metabolic syndrome, digestive and bone disorders: a general overview. Animal 4, 899–920. https://doi.org/10.1017/S1751731110000200.

Lofthag-Hansen, S., Huumonen, S., Gröndahl, K., Gröndahl, H.-G., 2007. Limited cone-beam CT and intraoral radiography for the diagnosis of periapical pathology. Oral Surg. Oral Med. Oral Pathol. Oral Radiol. Endod. 103, 114–119. https://doi.org/10.1016/j.tripleo.2006.01.001.

Martin, R.B., Boardman, D.L., 1993. The effects of collagen fiber orientation, porosity, density, and mineralization on bovine cortical bone bending properties. J. Biomech. 26, 1047–1054.

McGovern, J.A., Griffin, M., Hutmacher, D.W., 2018. Animal models for bone tissue engineering and modelling disease. Dis. Model. Mech. 11 https://doi.org/10.1242/dmm.033084.

McPhee, S., Groetsch, A., Shephard, J.D., Wolfram, U., 2021. Heat impact during laser ablation extraction of mineralised tissue micropillars. Sci. Rep. 11 https://doi.org/10.1038/S41598-021-89181-9.

Van Meerbeek, B., Willems, G., Celis, J.P., Roos, J.R., Braem, M., Lambrechts, P., Vanherle, G., 1993. Assessment by nano-indentation of the hardness and elasticity of the resin-dentin bonding area. J. Dent. Res. 72, 1434–1442. https://doi.org/10.1177/00220345930720101401.

Meredith, N., 1998. A review of nondestructive test methods and their application to measure the stability and osseointegration of bone anchored endosseous implants. Crit. Rev. Biomed. Eng. 26, 275–291. https://doi.org/10.1615/CritRevBiomedEng.v26.i4.20.

J Merheb, M. Vercruyssen, W. Coucke, M. Quirynen, K.U. Leuven, Relationship of implant stability and bone density derived from computerized tomography images, (n.d.). https://doi.org/10.1111/cid.12579.

Molly, L., 2006. Bone density and primary stability in implant therapy. Clin. Oral Implants Res. 17, 124–135. https://doi.org/10.1111/j.1600-0501.2006.01356.x.

Müller, M., 2006. Introduction to Confocal and Fluorescence Microscopy, second ed. SPIE, Bellingham, WA.

Nackaerts, O., Jacobs, R., Horner, K., Zhao, F., Lindh, C., Karayianni, K., van der Stelt, P., Pavitt, S., Devlin, H., 2007. Bone density measurements in intra-oral radiographs. Clin. Oral Invest. 11, 225–229. https://doi.org/10.1007/s00784-007-0107-2.

Norton, M.R., Gamble, C., 2001. Bone classification: an objective scale of bone density using the computerized tomography scan. Clin. Oral Implants Res. 12, 79–84. https://doi.org/10.1034/j.1600-0501.2001.012001079.x.

Nunoya, T., Shibuya, K., Saitoh, T., Yazawa, H., Nakamura, K., Baba, Y., Hirai, T., 2007. Use of miniature pig for biomedical research, with reference to toxicologic studies. J. Toxicol. Pathol. 20, 125–132. https://doi.org/10.1293/tox.20.125.

Nyman, J.S., Makowski, A.J., Patil, C.A., Masui, T.P., O'Quinn, E.C., Bi, X., Guelcher, S. A., Nicollela, D.P., Mahadevan-Jansen, A., 2011. Measuring differences in compositional properties of bone tissue by confocal Raman spectroscopy. Calcif. Tissue Int. 89, 111–122. https://doi.org/10.1007/s00223-011-9497-x.

Oh, J.-S., Kim, S.-G., 2012. Clinical study of the relationship between implant stability measurements using Periotest and Osstell mentor and bone quality assessment, Oral Surgery, Oral Medicine. Oral Pathol. Oral Radiol. 113, e35 https://doi.org/10.1016/j.tripleo.2011.07.003 e40.

Oja, H., 2010. Multivariate Nonparametric Methods with R. Springer New York, New York, NY. https://doi.org/10.1007/978-1-4419-0468-3.

Oliver, W.C., Pharr, G.M., 1992. An improved technique for determining hardness and elastic modulus using load and displacement sensing indentation experiments. J. Mater. Res. 7, 1564–1583. https://doi.org/10.1557/JMR.1992.1564.

Otsu, N., 1979. A threshold selection method from gray-level histograms. IEEE Trans. Syst. Man Cybernet. 9, 62–66. https://doi.org/10.1109/TSMC.1979.4310076.

Ovesy, M., Benjamin Voumard, ·, Zysset, P., 2018. A nonlinear homogenized finite element analysis of the primary stability of the bone-implant interface. Biomech. Model. Mechanobiol. 17, 1471–1480. https://doi.org/10.1007/s10237-018-1038-3.

O'Shea, D.C., Bartlett, M.L., Young, R.A., 1974. Compositional analysis of apatites with Laser-Raman spectroscopy: (OH,F,Cl)apatites. Arch. Oral Biol. 19, 995–1006. https://doi.org/10.1016/0003-9969(74)90086-7.

Peruzzi, C., Ramachandramoorthy, R., Groetsch, A., Casari, D., Grönquist, P., Rüggeberg, M., Michler, J., Schwiedrzik, J., 2021. Microscale compressive behavior of hydrated lamellar bone at high strain rates. Acta Biomater. 131, 403–414. https://doi.org/10.1016/j.actbio.2021.07.005.

Peter, K.L.H., McAnulty, A., Dayan, Anthony D., 2011. Niels-Christian Ganderup, the Minipig in Biomedical Research. CRC Press.

R core team, R, 2021. A Language and Environment for Statistical Computing.

Recker, R.R., Janet Barger-Lux, M., 2004. The Elusive Concept of Bone Quality.

Ribeiro-Rotta, R.F., Lindh, C., Pereira, A.C., Rohlin, M., 2011. Ambiguity in bone tissue characteristics as presented in studies on dental implant planning and placement: a systematic review. Clin. Oral Implants Res. 22, 789–801. https://doi.org/10.1111/j.1600-0501.2010.02041.x.

Roschger, A., Gamsjaeger, S., Hofstetter, B., Masic, A., Blouin, S., Messmer, P., Berzlanovich, A., Paschalis, E.P., Roschger, P., Klaushofer, K., Fratzl, P., 2014. Relationship between the v2PO4/amide III ratio assessed by Raman spectroscopy and the calcium content measured by quantitative backscattered electron microscopy in healthy human osteonal bone. J. Biomed. Opt. 19, 065002 https://doi.org/10.1117/1.jbo.19.6.065002.

Rosol, T.J., Tannehill-Gregg, S.H., LeRoy, B.E., Mandl, S., Contag, C.H., 2003. Animal models of bone metastasis. Cancer 97, 748–757. https://doi.org/10.1002/cncr.11150.

van Rossum, G., Drake, F.L., 2009. Python 3 Reference Manual. CreateSpace., Scotts Valley, CA.

Rozkot, B.J., M, Václavková, E., 2015. Minipigs as laboratory animals - review. Res. Pig Breed. 2015, 10–14.

Ruehe, B., Niehues, S., Heberer, S., Nelson, K., 2009. Miniature pigs as an animal model for implant research: bone regeneration in critical-size defects. Oral Surg. Oral Med. Oral Pathol. Oral Radiol. Endod. 108, 699–706. https://doi.org/10.1016/j.tripleo.2009.06.037.

Salehi, H., Terrer, E., Panayotov, I., Levallois, B., Jacquot, B., Tassery, H., Cuisinier, F., 2012. Functional mapping of human sound and carious enamel and dentin with Raman spectroscopy. J. Biophot. https://doi.org/10.1002/jbio.201200095 n/a-n/a.

Scarfe, W.C., Farman, A.G., Sukovic, P., 2006. Clinical applications of cone-beam computed tomography in dental practice. J. Can. Dent. Assoc. 72, 75–80.

Schwiedrzik, J., Raghavan, R., Bürki, A., Lenader, V., Wolfram, U., Michler, J., Zysset, P., 2014. In situ micropillar compression reveals superior strength and ductility but an absence of damage in lamellar bone. Nat. Mater. 13, 740–747. https://doi.org/10.1038/nmat3959.

Schwiedrzik, J., Taylor, A., Casari, D., Wolfram, U., Zysset, P., Michler, J., 2017. Nanoscale deformation mechanisms and yield properties of hydrated bone extracellular matrix. Acta Biomater. 60, 302–314. https://doi.org/10.1016/j.actbio.2017.07.030.

M. Shahlaie, B. Gantes, E. Schulz, M. Riggs, M. Crigger, Bone density assessments of dental implant sites: 1. Quantitative computed tomography., Int. J. Oral Maxillofac. Implants. 18 (n.d.) 224–231.

Sietsema, W.K., 1995. Animal models of cortical porosity. Bone 17, S297–S305. https://doi.org/10.1016/8756-3282(95)00307-Y.

Simmons, J.K., Hildreth, B.E., Supsavhad, W., Elshafae, S.M., Hassan, B.B., Dirksen, W.P., Toribio, R.E., Rosol, T.J., 2015. Animal models of bone metastasis. Vet. Pathol. 52, 827–841. https://doi.org/10.1177/0300985815586223.

Smith, M., 2009. ABAQUS/Standard User's Manual, Version 6.9. Dassault Systèmes Simulia Corp, Providence, RI.

Stoppie, N., Pattijn, V., Van Cleynenbreugel, T., Wevers, M., Vander Sloten, J., Naert, I., 2005. Structural and radiological parameters for the characterization of jawbone. Comput. Methods Biomech. Biomed. Eng. 8, 261–262. https://doi.org/10.1080/10255840512331389253.

Tertuliano, O.A., Greer, J.R., 2016. The nanocomposite nature of bone drives its strength and damage resistance. Nat. Mater. 15, 1195–1202. https://doi.org/10.1038/nmat4719.

Turkyilmaz, I. (Ed.), 2011. Implant Dentistry: the Most Promising Discipline of Dentistry. InTech.

Uchic, M.D., Dimiduk, D.M., 2005. A methodology to investigate size scale effects in crystalline plasticity using uniaxial compression testing. Mater. Sci. Eng. 400–401, 268–278. https://doi.org/10.1016/j.msea.2005.03.082.

V Swain, M., Xue, J., 2009. State of the art of micro-CT applications in dental research. Int. J. Oral Sci. 1, 177–188. https://doi.org/10.4248/IJOS09031.

Vitulli, I., Fontenele, R.C., Nascimento, E.H.L., Freitas, D.Q., 2022. Influence of artefacts generated by titanium and zirconium implants in the study of trabecular bone architecture in cone-beam CT images. Dentomaxillofacial Radiol. https://doi.org/10.1259/dmfr.20220066.

Vodička, P., Smetana, K., Dvořánková, B., Emerick, T., Xu, Y.Z., Ourednik, J., Ourednik, V., Motlík, J., 2005. The miniature pig as an animal model in biomedical research. Ann. N. Y. Acad. Sci. 1049, 161–171. https://doi.org/10.1196/annals.1334.015.

Voumard, B., Maquer, G., Heuberger, P., Zysset, P.K., Wolfram, U., 2019. Peroperative estimation of bone quality and primary dental implant stability. J. Mech. Behav. Biomed. Mater. 92, 24–32. https://doi.org/10.1016/j.jmbbm.2018.12.035.

Wang, Y., Spencer, P., Walker, M.P., 2007a. Chemical profile of adhesive/caries-affected dentin interfaces using Raman microspectroscopy. J. Biomed. Mater. Res., Part A 81, 279–286. https://doi.org/10.1002/JBM.A.30981.

Wang, S., Liu, Y., Fang, D., Shi, S., 2007b. The miniature pig: a useful large animal model for dental and orofacial research. Oral Dis. 13, 530–537. https://doi.org/10.1111/j.1601-0825.2006.01337.x.

Watanabe, K., Lewis, S., Guo, X., Ni, A., Lee, B.S., Deguchi, T., Kim, D.G., 2020. Regional variations of jaw bone characteristics in an ovariectomized rat model. J. Mech. Behav. Biomed. Mater. 110, 103952 https://doi.org/10.1016/J.JMBBM.2020.103952.

Weaver, M.E., Sorenson, F.M., Jump, E.B., 1962. The miniature pig as an experimental animal in dental research. Arch. Oral Biol. 7 https://doi.org/10.1016/0003-9969(62)90044-4.

Weber, R., Graf, T., Berger, P., Onuseit, V., Wiedenmann, M., Freitag, C., Feuer, A., 2014. Heat accumulation during pulsed laser materials processing. Opt Express 22, 11312. https://doi.org/10.1364/OE.22.011312.

Weber, R., Graf, T., Freitag, C., Feuer, A., Kononenko, T., Konov, V.I., 2017. Processing constraints resulting from heat accumulation during pulsed and repetitive laser materials processing. Opt Express 25, 3966. https://doi.org/10.1364/OE.25.003966.

White, S., Atchison, K., Gornbein, J., Nattiv, A., Paganini-Hill, A., Service, S., Yoon, D., 2005. Change in mandibular trabecular pattern and hip fracture rate in elderly women. Dentomaxillofacial Radiol. 34, 168–174. https://doi.org/10.1259/dmfr/32120028.

von Wowern, N., 2001. General and oral aspects of osteoporosis: a review. Clin. Oral Invest. 5, 71–82. https://doi.org/10.1007/s007840100105.

Zeileis, A., Hothorn, T., 2002. Diagnostic checking in regression relationships. R. News 3, 7–10.

Zhang, H., Schuster, B.E., Wei, Q., Ramesh, K.T., 2006. The design of accurate micro-compression experiments. Scripta Mater. 54, 181–186. https://doi.org/10.1016/j.scriptamat.2005.06.043.

Zysset, P.K., Edward Guo, X., Edward Hoffler, C., Moore, K.E., Goldstein, S.A., 1999. Elastic modulus and hardness of cortical and trabecular bone lamellae measured by nanoindentation in the human femur. J. Biomech. 32, 1005–1012. https://doi.org/10.1016/S0021-9290(99)00111-6.